RESEARCH ARTICLE

Analysis of turbulent flow structures in the straight rectangular open channel with floating vegetated islands

Xuecheng Fu [1] · Feifei Wang [1] · Mengyang Liu [1] · Wenxin Huai [1]

Abstract
Floating vegetated islands (FVIs) are extensively implemented in various river ecology restoration projects, given their capability of decontaminating pollutants. The fluid dynamical behaviors of turbulence through FVIs are studied in the flume by using the SonTek Acoustic Doppler Velocimetry. Through conventional spectral and quadrant analyses, flow characteristics, such as energy content and turbulent momentum exchange, are investigated as the flow encountered a series of root canopies. A shear layer with corresponding coherent vortex structures at the bottom of root canopies occurred, which is generated by Kelvin–Helmholtz instabilities. These instabilities are usually derived from velocity differences between root canopy and gap region. Shear- and stem-scale vortices are identified by using spectral analysis. The power spectral density function on measured vertical velocity fluctuations in the flow direction near the bottom of root canopies from the leading edge of FVIs is computed. Given the flow developing downstream, a series of the spectral curves has gradually showed one dominant dimensionless frequency at 0.046. The sweep and ejection events have contributed prominently to the Reynolds stress in whole vertical direction. Momentum flux carried by sweeps outweighs its counterpart carried by ejections inside root canopies. However, the situation is different outside root canopies. The sweep–ejection contributions are brief but crucial to the total turbulent momentum exchange, which is in good agreement with considerable studies on turbulent flow through canopies.

Keywords Floating vegetated islands · Coherent vortex structures · Quadrant analysis · Spectral analysis

Highlights
Turbulence characteristics, including momentum thickness, velocity, and the Reynolds stress distribution, were studied.
Power spectral density analysis was used to explore vortex structures.
Quadrant analysis was adopted to elucidate momentum transporting properties of vortices.

Responsible editor: Philippe Garrigues

✉ Wenxin Huai
  wxhuai@whu.edu.cn

  Xuecheng Fu
  xuechengfu@whu.edu.cn

  Feifei Wang
  ffwang1991@whu.edu.cn

  Mengyang Liu
  liumy@whu.edu.cn

[1] State Key Laboratory of Water Resources and Hydropower Engineering Science, Wuhan University, Wuhan 430072, Hubei, China

Introduction

Floating aquatic plants grow on water surface with buoyant stems and unanchored roots (Nahlik and Mitsch 2006; Downing-Kunz and Stacey 2011). In an aquatic system, a floating vegetated island (FVI) is composed of free-floating macrophytes and floating organic materials placed in a specific matrix on water surface (Nichols et al. 2016). The three components of FVIs serve various ecological functions. First, the specific matrix provides strength and buoyance to support and anchor the island floating on water surface. Second, root canopies under water surface assimilate pollutants not only through physical processes but also through chemical processes, including filtration, adhesion, and nutrient uptake. These chemical processes are conducive to the improvement of water quality. Third, leaf canopies above the matrix can beautify the environment and provide habitats for small animals that live on land (Fig. 1). Realizing the functions of FVIs, several engineers built artificial vegetated treatment wetlands to imitate the functions of natural FVIs in wastewater treatment and polluted pond recovery (Keddy

Fig. 1 Photo and schematic of FVI system

2010; Liu et al. 2019). Such islands are proven to be economical and environmentally friendly, given that earthwork or land occupation is unnecessary (Stewart et al. 2008; Borne 2014). The environmental protection functions the FVIs serve include physical, chemical, and biological processes and their interactions (Nikora 2010). However, most studies have concentrated on purification capacity of FVIs in wastewater treatment, namely, chemical and biological processes. For instance, Borne (2014) has demonstrated that FVIs effectively remove total suspended solids. Tanner et al. (2011) have shown that FVIs reduce total suspended solids by 81%, total nitrogen by 34%, and total phosphorus by 19%. These research findings have demonstrated the capability of FVIs to decrease pollutants, which vary with the flow inlet, flow velocity, and inflow discharge. However, only few studies have aimed to investigate the flow regime in FVIs, that is, the physical process. Providing deep insights on such physical process will enhance the appreciation of the interplay among all kinds of processes and link all these disciplines together (Lin et al. 2002; Toft et al. 2003). Physical studies on hydrophytes concentrate on either emergent or submerged canopies rather than FVIs. The root canopy of FVIs represents suspended canopy with the drag force extending downward from water surface. The suspended canopy is different from the submerged canopy, given that the decrease in velocity occurs in canopies and near the channel bed; thus, the maximum flow velocity occurs in the gap region between canopies and the channel bed (Plew et al. 2006; Ai et al. 2020).

Research findings on model canopy of emergent and submerged aquatic plants have demonstrated that a layer of increase in velocity shear grows at the interface between canopies and the free flow, in which the mixing layer is created (Ghisalberti and Nepf 2004; White and Nepf 2007). The mixing layer is characterized by an inflection point in streamwise velocity profiles, which results in coherent vortices that exchange momentum through the interface between canopies and the free flow at higher rates than the traditional boundary layer (Raupach et al. 1996; Li et al. 2019). This elevated transport leads to the intensive influence of aquatic plants on environmental processes, such as sediment transport, dissolved oxygen content, and nutrient and metal uptake.

Compared with emergent and submerged aquatic canopies, few studies have been conducted on the hydrodynamic interactions in the root canopies of FVIs. However, research findings on other types of suspended aquatic canopy may serve as references, which indicate the growth of the mixing layer. In an experiment, Plew (2011) has divided three vertical layers of flow in the suspended canopies model: one bottom boundary layer (BBL) near the channel bed; one canopy shear layer, which penetrates a part of suspended root canopy from the top of BBL to the penetration depth; and one internal canopy layer, which is located in suspended root canopies over the canopy shear layer. Moreover, hydrodynamic interaction is ecologically significant for FVIs. For instance, biological uptake in root canopies eventually affects ecological processes (e.g., nutrient and metal removal), which are controlled by the reaction kinetics and mass transfer process (Sanford and Crawford 2000). The mass transfer process is controlled by the flux of nutrients into the root canopies, which are dominated by hydrodynamic interactions. The turbulent structures and change of turbulent intensity have a certain influence on the transport of suspended solids and pollutants in the flow. And a greater comprehension of root canopy hydrodynamics may help increase the removal efficiency of FVIs in phytoremediation. Meanwhile, understanding the interaction between hydrodynamics and root canopies is essential to the numerical modeling of ecosystems with large populations of FVIs. Thus, studying the hydrodynamic interactions through the root canopy of FVIs is relevant.

The purpose of this study is to explore the mean flow and turbulent structures inside and under root canopies of FVIs with a concentration on momentum transport. The spatial development and vertical structure of velocity are investigated by utilizing high-frequency velocity measurements. Traditional spectral and quadrant analyses are also applied to

Fig. 2 Experimental setup showing the placement of FVIs in the flume

determine scales and vertical momentum transport between root canopy and gap region.

Experimental setup

The experiments were conducted in a 20 m-long, 1 m-wide (B) glass flume with a bed slope of $S_0 = 0.01\%$ (see Fig. 2). The water depth was controlled using the tailgate to obtain a steady uniform state, whereas the discharge was measured by an electromagnetic flowmeter installed in front of the flume. The flow went through a flow straightener mounted on the entrance of the flume, generating a laterally uniform velocity profile. A channel flow rate of $Q = 0.042$ m³/s and a water depth of $H = 0.43$ m were applied. The cross-sectional average streamwise velocity was $U_m = 0.097$ m/s. The flow was

turbulent given the bulk Reynolds number $Re = U_m H/\nu = 4.15 \times 10^4$ with the water depth H and kinematic viscosity ν (10^{-6} m²/s). The bulk Froude number Fr ($U_m/\sqrt{gH}$) was 0.047, indicating that the flow was subcritical with gravitational acceleration g.

Several sets of rigid cylinders were assembled to simulate floating macrophyte roots (Fig. 3). These cylinders were arranged orthogonally with side length of the square element $s = 0.05$ m. The height and diameter of these cylinders were $h_r = 0.25$ m and $d = 0.006$ m, respectively. Beneath root canopy, the height of the gap region was $h_g = 0.18$ m. Based on the definition of terrestrial canopies, the root canopy density was defined as the frontal area per root volume $a = nd = 2.4$ m⁻¹, where n represents the number of cylinders per bed area (Nepf and Vivoni 2000). The cylinders were fixed vertically on several polyvinyl chloride (PVC) boards hung up on the same

Fig. 3 Sketches of laboratory flume with the placement of FVIs. **a** Schematic top view of FVIs (denoted as gray box) in the center of the flume; B is the width of the flume, whereas b is the width of FVIs. L_{veg} is the total length of FVIs. **b** Schematic diagram of vegetation elements with diameter d and spacing s. **c** Side view of the flume and FVIs with water depth H, root canopy height h_r, and gap height h_g
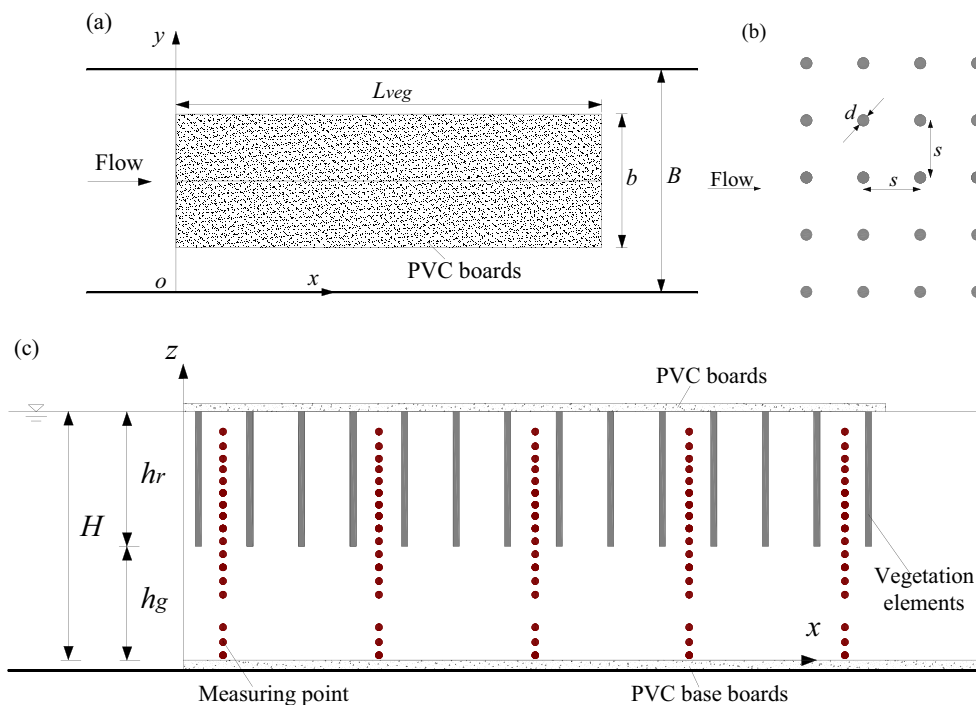
horizontal plane. The length and width of each board were 1.0 m and 0.3 m, respectively. The boards were placed side by side downstream with the adjacent boundary line between two boards aligned with the center line of the flume. As shown in Fig. 3a, the total length and width of the FVIs were L_{veg} = 5 m and b = 0.6 m, respectively. Several PVC baseboards (2 m length × 1 m width × 0.01 m thickness) were used to cover the bottom of the flume with the leading edge set at x = 0, which started from 9 m away from the flume entrance.

The streamwise coordinate corresponded to x, with x = 0 set at the leading edge of root canopy. The lateral coordinate corresponded to y, with y = 0 set at the right wall of the channel (looking downstream). The vertical coordinate corresponded to z, with z = 0 set at the top of the PVC baseboards (Fig. 3). The corresponding velocity vector components are $\boldsymbol{u}(x, y, z)$ = (u, v, w). The velocity was measured using the SonTek Acoustic Doppler Velocimetry (ADV) with the recording period of 160 s at the frequency of 50 Hz. The signal strength of velocity components and correlation were mainly used to show the accuracy of the velocity measuring data. The "raw" velocity components data were proven by high levels of noise and spikes (Nikora and Goring 1998). The ADV velocity time series described the effects of the velocity fluctuations, Doppler noise, installation constraints, signal aliasing, and other disturbances. The dataset was primarily "cleaned" by excluding low signal-to-noise ratio (< 15) and low-correlation (< 70%) samples and removing "spikes" using the method of Goring and Nikora (2002). Given that the velocities were measured at one location in y, the lateral variability of velocity field was not assessed. Then, 14 measuring vertical lines were arranged in the longitudinal direction in the middle of FVIs. Each perpendicular had 17–22 measure points with vertical distance between two adjacent ones at 0.02–0.06 m. The results obtained were used to analyze the detailed turbulent structures in the interface between root canopy and gap region.

Results and discussions

The results and discussions were organized as follows. In "Mean flow and turbulent characteristics," the domain where turbulent flow structures and the mean flow were in equilibrium with the root canopy was identified. Moreover, three longitudinal regions were classified based on the flow characteristics. Then, the vertical profiles of the time-averaged longitudinal velocity, Reynolds stress, and turbulent kinetic energy (T_{KE}) at fully developed flow region were discussed. In "Power spectral density analysis," the energy content and frequencies of the dominant vortices were studied by using longitudinal and vertical directions to determine vortices of different scales in various locations. The power–spectral density analysis was used in this study to estimate the fluctuations of

the single velocity component. In "Quadrant analysis," the vertical momentum transport property of vortices was studied by using quadrant analysis with one hyperbolic "hole" conditional sampling to determine the varying contributions of momentum transport events. The momentum contributions of coherent structures with corresponding duration were determined in the end.
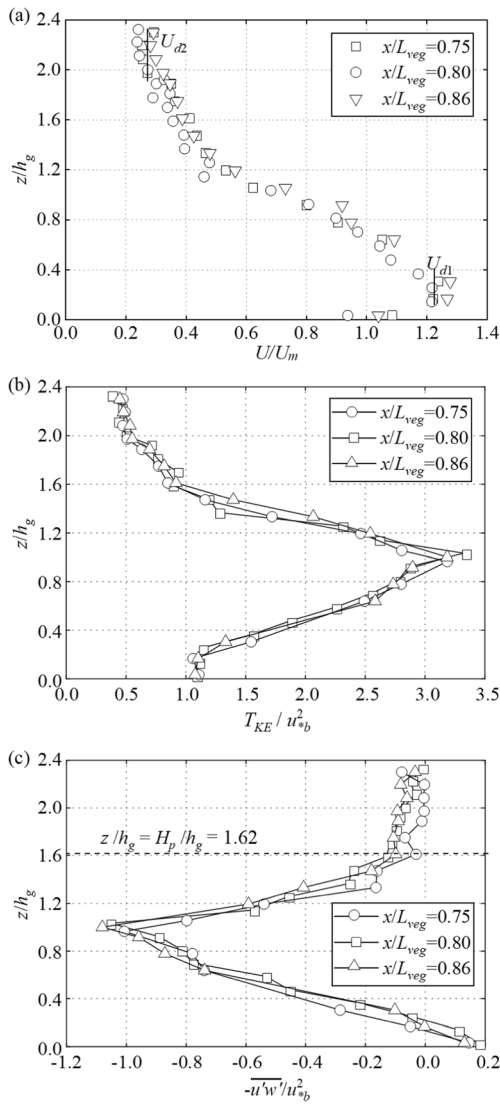
The data shown in following figures were normalized by geometric and flow variables. Except as otherwise noted, the longitudinal distance (x) was normalized using the length of FVIs (L_{veg}). The vertical distance (z) was also normalized using the height of gap region h_g resulting in $0 < z/h_g < 1$ being the gap region, and $1 < z/h_g < 2.4$ being the root canopy. Velocities were normalized using cross-sectional average streamwise velocity of the flow U_m, whereas the Reynolds stresses were normalized using a bulk friction velocity $u_{*_b} \sqrt{gR_H S_0}$, where $R_H = BH/(B + b + 2H)$ was the hydraulic radius based on the cross sectional area (BH) and wetted perimeter ($B + b + 2H$) in the absence of root canopy.

Mean flow and turbulent characteristics

The vertical distributions of measured time-averaged streamwise velocity at three different longitudinal locations (x/L_{veg} = 0.75, x/L_{veg} = 0.80, and x/L_{veg} = 0.86) are shown in Fig. 4a, which also exhibits three vertical regions. Velocity remained stable in the upper layer of root canopy. Then, velocity increased in the lower layer of root canopy and in the upper layer of gap region. Finally, velocity reached its maximum value between the lower layer of gap region and channel bed, then decreased dramatically toward the bottom. The maximum velocity was approximately 1.22 U_m. The Reynolds stresses and T_{KE} were altered due to the existence of root canopies as expected. T_{KE} value was primarily used to describe the intensity of turbulence, which can be formulated as:

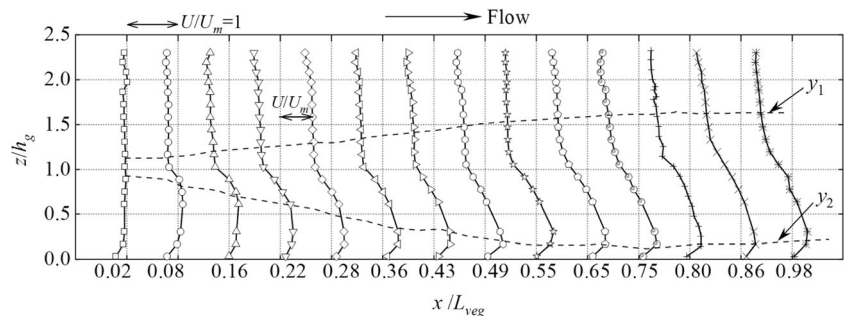$$T_{KE} = \left(\overline{u'^2} + \overline{v'^2} + \overline{w'^2} \right)/2 \tag{1}$$

T_{KE} profiles at three different longitudinal locations (x/L_{veg} = 0.75, x/L_{veg} = 0.80, and x/L_{veg} = 0.86) are shown in Fig. 4b. Similar as the time-averaged streamwise velocity profiles, T_{KE} profile varied appreciably. T_{KE} profile reached the maximum value near the water–canopy interface and decreased toward the top of root canopy and the bottom of the channel, indicating that T_{KE} mainly came from the shear layer at the bottom of root canopy. The turbulent shear stresses "invaded" the root canopies, which led to strong vertical momentum exchange near the water–canopy interface. The penetration depth $z = H_p$ was defined as the depth at which the shear stresses in root canopies decreased to approximately 10% of the maximum turbulent shear stress, as shown in Fig. 4c (Nepf and Vivoni 2000). The first peak of the Reynolds stresses appearing at the

Fig. 4 Experimental results in the fully developed region. **a** Vertical distribution of time-averaged streamwise velocity. **b** Vertical distribution of normalized T_{KE}. **c** Vertical distribution of the normalized Reynolds stresses

root canopy) and the bottom of the flume. The second peak was observed inside the gap region near the channel bed with a positive sign, which is contrary to the former. Inside root canopy, the Reynolds stresses approached zero above the penetration depth $z/h_g = H_p/h_g = 1.62$, wherein the gravitational force was only in balance with the drag of vegetation. Thus, the value of the streamwise velocity was determined. The negative Reynolds stress peak of this study at the water–canopy interface was contrary to the sign of submerged canopy in the same place, given that their streamwise velocity gradients in the vertical direction were opposite.

Next, the longitudinal development of the time-averaged streamwise velocity profiles should be discussed. Figure 5 exhibits the vertical distribution of the time-averaged longitudinal velocities and growth of the mixing layer with the increasing distance starting from the leading edge of root canopies. The mixing layer is contained in the width from the top of the BBL to the penetration depth H_p, wherein the distance from the channel bed to the points of zero $-\overline{u'w'}$ is used to define the bottom boundary layer thickness (Plew 2011). As shown in Fig. 5, the development of flow through root canopy has three regions:

(1) The first one was the initial fluid adjustment region in the entrance of root canopies. Fully uniformed vertical distributions of time-averaged streamwise velocities were hardly achieved immediately, given that the fluid encountered FVIs ($x = 0$) on account of the existence of upstream pressure effects deriving from the resistance the canopy roots serve. In this region, the streamwise velocities in root canopies decreased and the outward flux occurred strongly near the water–canopy interface owing to the drag force that the root canopies serve. The velocity differences in the vertical direction induced the shear layer at the inlet of FVIs. In this shear layer, vortices of small scale appeared and then evolved downstream. The initial adjustment was completed when the vertical velocity at the bottom of the root canopy stayed stable (approaching zero) and the streamwise velocity in the root canopy remained unchanged. As shown in Fig. 6a, the initial fluid adjustment region can be regarded as the adjustment of the average velocity of the root canopy.

water–canopy interface was obvious, indicating the strong shear effect. However, the Reynolds stresses declined toward the top of root canopy (due to the momentum absorption by

Fig. 5 Vertical distributions of time-averaged longitudinal velocities with increasing x from the leading edge of the root canopy; the width of mixing layer is shown by two dashed lines, y_1 and y_2

Its length can be determined by the vertical velocity at the bottom of the root canopy. The length of initial adjustment region was approximately $0.3\ L_{veg}$. The vertical velocity value remained stable at -0.002 m/s, which was not zero due to acoustic streaming when using ADV measurement (Poindexter et al. 2011).

(2) The second one was the developing region, wherein the shear layer had penetrated the root canopy. Moreover, the width of mixing layer near the water–canopy interface gradually increased and finally reached equilibrium. The shape of the mixing layer resembled a slim sector, indicating development of the shear layer. Figure 6b describes the growth of momentum thickness θ and the development of the mixing layer at various locations in longitudinal direction, which increased rapidly and remained unchanged after approximately $x/L_{veg} = 0.75$ (recall that the previous analyses of the turbulent stress and time-averaged streamwise velocity were conducted after $x/L_{veg} = 0.75$). After achieving this value, the width of mixing layer almost achieved stability and became independent of x.

(3) The third one was the fully developed region, in which the turbulent structure was completely formed and the streamwise velocity profiles remained roughly unchanged (i.e., $\partial U/\partial x = 0$). The mixing layer was well developed and its development was nearly irrelevant to x. The layer below the mixing layer was adjusted according to the boundary condition and kept balance with the existence of root canopies.

The expression of momentum thickness was adopted from the study of Rogers and Moser (Rogers and Moser 1994) and modified with the range of integration from the top of BBL to the water surface, which can be formulated as:

$$\theta = \theta_1 + \theta_2 = \int_{z_{BBL}}^{H} \left[\frac{1}{4} - \left(\frac{U - \langle U \rangle}{\Delta U} \right)^2 \right] dz \quad (2)$$

where θ_1 and θ_2 are two momentum thickness components in the high- and low-stream velocity layers, respectively. The velocity $\langle U \rangle$ is arithmetic average of U_{d1} and U_{d2}, namely, $\langle U \rangle = (U_{d1} + U_{d2})/2$. U_{d1} and U_{d2} are stable time-averaged streamwise velocities in high- and low-stream velocity layers, respectively. The velocity difference ΔU is calculated from $\Delta U = U_{d1} - U_{d2}$. The typical width of mixing layer has continued to develop downstream in the free shear layer. However, the development of mixing layer is expected to be limited by boundary conditions, namely, the depth of water and flume bottom. In the fully developed region ($0.75 < x/L_{veg} < 1$), the momentum thickness and the width of mixing layer have reached stability at 0.03 m and 0.236 m, respectively. A correlation is observed between the two values, $\theta = (0.12 \pm 0.02)\delta$. This finding is consistent with Plew (2011).

Power spectral density analysis

The shear layer near the water–canopy interface was induced by the velocity difference. In this shear layer, coherent vortex structure spreading downstream was produced by Kelvin–Helmholtz instability, which was also the reason for the generation of the mixing layer. Some studies in turbulent canopies have documented coherent vortices resulting from a Kelvin–Helmholtz instability initiated by the strong shear and velocity inflection at the water–canopy interface (Raupach et al. 1996; Ghisalberti and Nepf 2002). The coherent structures enhanced scalar and momentum exchange, carrying high–momentum fluid into the canopy from below. The size of the vortex structure grew continuously with the increasing value of x and eventually led to equilibrium ($x/L_{veg} > 0.75$) until the dissipation term of T_{KE} was balanced by the mechanical and wake production generation terms. The vortices dominated the vertical energy content and momentum exchange and induced the periodic fluctuation of velocities near the water–canopy interface. The coherent vortex structures can be identified by the periodic fluctuation of longitudinal and vertical velocity component time series. Figure 6 presents the representative time series of the instantaneous streamwise velocity u and instantaneous vertical velocity w near the water–canopy interface at a representative cross-section ($x/L_{veg} = 0.80$). Due to the special arrangement position of FVIs (the time-averaged streamwise velocity gradient was negative), the relationship

Fig. 6 Experimental results along the streamwise direction. **a** Development of time-averaged vertical velocity W in the longitudinal direction at the bottom of the root canopy ($z/h_g = 1.06$). **b** Growth of the momentum thickness and the mixing layer downstream from the beginning of the root canopy
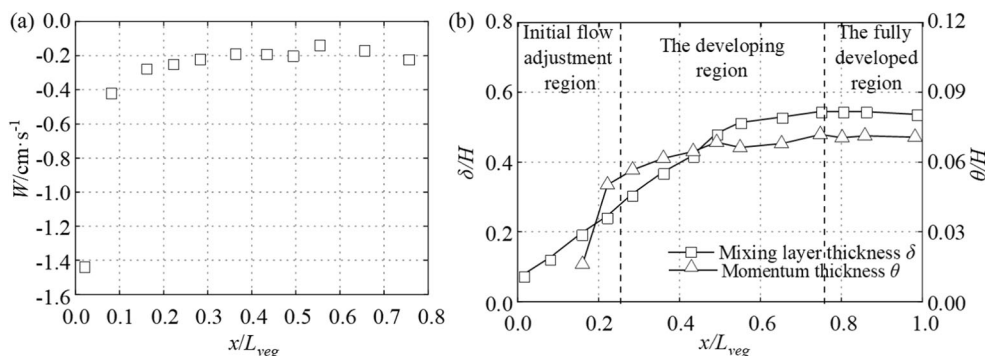
between the fluctuations of streamwise and vertical velocities was positively correlated. This finding showed the strong vertical momentum exchange.

As mentioned above, a coherent vortex structure was created by the root canopy and had induced periodic velocity fluctuations at the bottom of root canopies, which then dominated vertical momentum exchange (as shown in Fig. 7). To examine the frequency of vortex spreading, spectral analysis was applied to analyze the vertical fluctuating velocity w' at the bottom of root canopies.

As shown in Fig. 8, the power spectral density of vertical velocity fluctuations near the bottom and inside of the root canopy was computed to explain the effects of various vortices. To convert the velocity signal in wave form to the power carried by wave per unit frequency, the fast Fourier transform of the vertical velocity fluctuations was performed. The Welch method was used for spectrum analysis in this study (Welch 1967). The energy spectrum had three sub-regions: the large-scale coherent vortex, shear production, and inertial sub-regions. The coherent vortex structures in large-scale region assumed a "bump." In the inertial sub-region, the power spectral density curves roughly satisfied the Kolmogorov turbulence spectrum with a − 5/3 power law at high-frequency range and the viscous dissipation was negligible.

The variation of power spectral density with frequency was described in power spectral density diagram (Fig. 8). The frequency corresponding to its peak can be regarded as the dominant frequency of the vortex. The dominant frequency at a given point near the bottom of root canopy ($z/h_g = 1.2$) was $f = 0.09$ Hz, whereas the counterpart was $f = 0.9$ Hz inside root canopy ($z/h_g = 2.0$). The Strouhal number (St) is suitable for describing the relationship between the characteristic length of the vortex size L and vortex shedding frequency f. St can be normalized as:

$$St = fL/U_a \tag{3}$$

where U_a is the characteristic streamwise velocity. In the subcritical region, $St = 0.21$ (Schlichting and Gersten 2017),
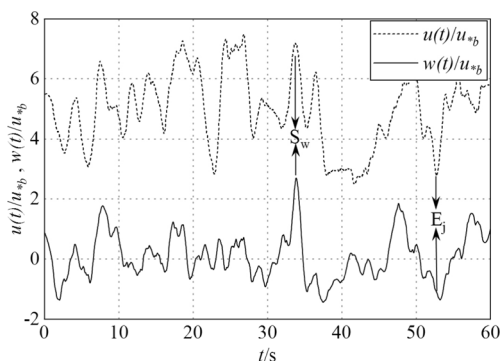
which was used to describe the dominant frequency in the velocity spectra inside cylindrical rods representing the rigid canopy (Poggi et al. 2004). At $z/h_g = 1.2$ (i.e., inside the shear layer), the dominant frequency f in the spectral analysis was approximately 0.09 Hz. Given the characteristic streamwise velocity $U_a = U_m = 0.097$ m/s and $St = 0.21$, the corresponding characteristic vortex length of 0.226 m was calculated. This length was in good agreement with the mixing layer thickness (0.236 m) in the fully developed flow region. This finding demonstrated that the vortices at the bottom of root canopy were restricted due to the existence of vegetation. At $z/h_g = 2.0$ (i.e., inside root canopy), f was 0.9 Hz and U_a was the approach velocity toward the obstacle near 0.03 m/s. Hence, $L = 0.007$ m was calculated, which approached the diameter of the single vegetated element $d = 0.006$ m. This finding demonstrated that the vortex at this point was mainly caused by the wake of an individual vegetated element. In sum, two types of vortices were observed dominating different areas, namely, shear-scale vortices (relative to the Kelvin–Helmholtz instabilities) and stem-scale vortices (relative to stem diameter and wakes).

Evidently, a single dominant frequency component may exist through the periodicity of fluctuations in streamwise and vertical velocity (Fig. 7). Thus, we aimed to explore this component longitudinally. The spectrum of vertical velocity fluctuations near the bottom of root canopies ($z/h_g = 1.06$) was calculated at a variety of streamwise places with its frequency normalized by the velocity $\langle U \rangle$ and momentum thickness $\theta(x)$ of each cross-section, as shown in Fig. 9. The peak in the power spectral density curves determined the dominant frequency of coherent vortex structure in the mixing layer. When the water flowed downstream, the energy was concentrated gradually. Then, the equilibrium was reached where almost overall energy was concentrated on one dominant frequency, which occurred at nearly the same streamwise place ($x/L_{veg} = 0.75$) as the equilibrium of the time-averaged streamwise velocity profiles (Fig. 5). The average spectral peak was $f\theta/\langle U \rangle = 0.046 \pm 0.005$.

Quadrant analysis

Quadrant analysis was used to analyze the turbulent structures responsible for the momentum exchange. This method was first adopted by Lu and Willmarth (1973) to explore the shear stress characteristics at the boundary layer, which was outside the turbulent viscous layer. In quadrant analysis, the Reynolds stresses are decomposed into four different flow types that are labeled as Q1, Q2, Q3, and Q4 in the u'–w' vertical plane based on the signs of fluctuating velocities. As shown in Figs. 10 and 12a, u' and w' represent streamwise and vertical fluctuating velocity, respectively. At a given point, due to the special arrangement position of FVIs (the time-averaged streamwise velocity gradient was negative, where 0.24 < z/

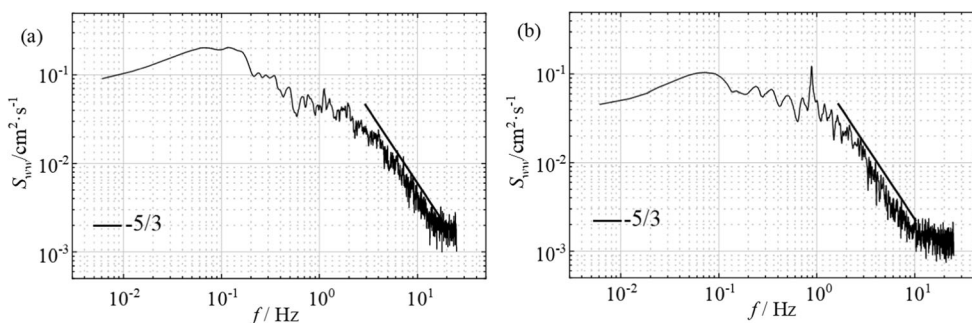
Fig. 7 Time series of instantaneous streamwise and vertical velocity components at a given point at the water–canopy interface in the fully developed flow region ($x/L_{veg} = 0.80$, $z/h_g = 1.06$)

Fig. 8 Power spectral density of vertical velocity fluctuations at two representative points in the fully developed flow region ($x/L_{veg} = 0.80$): **a** near the bottom of root canopy ($z/h_g = 1.2$) and **b** inside root canopy ($z/$ $h_g < 2.4$), these quadrants correspond to Q1 as the sweep event ($u' > 0$, $w' > 0$), indicating the upward movement of high-speed fluid; Q2 as the inward interaction ($u' < 0$, $w' > 0$), indicating the upward movement of low-speed fluid; Q3 as the ejection event ($u' < 0$, $w' < 0$), indicating the downward movement of low-speed fluid; and Q4 as the outward interaction ($u' > 0$, $w' < 0$), indicating the downward movement of the high-speed fluid. However, with regard to the region near the channel bed (the time-averaged streamwise velocity gradient was positive, where $0 < z/h_g < 0.24$), Q1 (inward interactions), Q2 (ejections), Q3 (outward interactions), and Q4 (sweeps) $h_g = 2.0$); the exponent of the line related to the locally homogeneous and isotropic turbulence predicted from Kolmogorov's theory is − 5/3

were defined similar with traditional boundary layer flows, as shown in Fig. 12b (Lu and Willmarth 1973; Raupach and Thom 1981).

Figure 10 presents a diagram of the four quadrants contributing to the momentum transport at a fixed point with a "hole" formed by four hyperbolae defined by $\left| u'w' \right| = H_0 \left| \overline{u'w'} \right|$, where H_0 was the threshold value representing the "hole" scale. The establishment of a "hole" region was important when removing the back-ground small events, given that large values of the Reynolds stresses in four quadrants can be extracted.

The contribution of various flow types to the local Reynolds stresses in Q_i quadrant can be calculated as:

$$S_{i,H_0} = \frac{1}{T}\int_0^T C_{i,H_0}(t)u'(t)w'(t)dt, \tag{4}$$
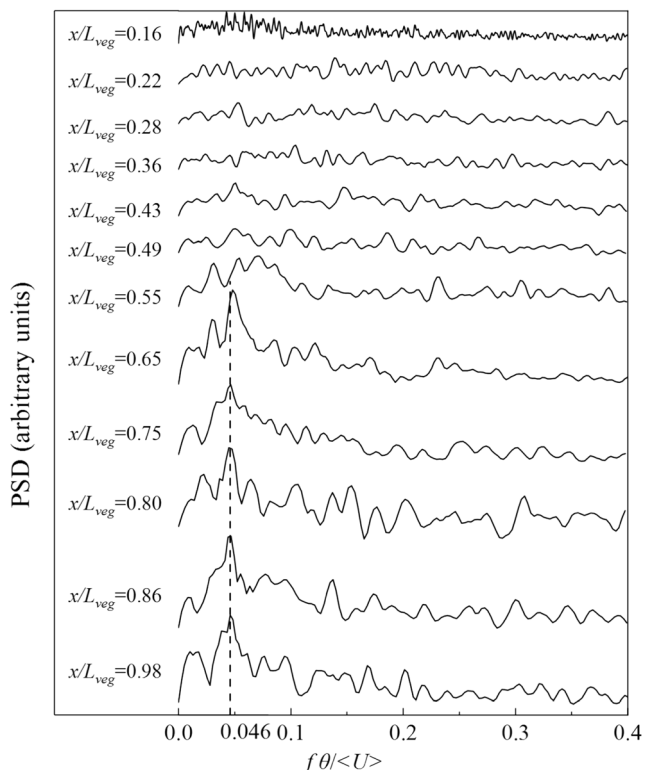
Fig. 9 The power spectral density for vertical velocity fluctuations near bottom of root canopies in different *x*-positions. Abscissae for the PSD plots are the normalized frequency, $f\theta/\langle U\rangle$. The dominant frequency $f\theta/\langle U\rangle = 0.046$ is shown by the dotted line. The magnitudes of the PSD curves are not shown.
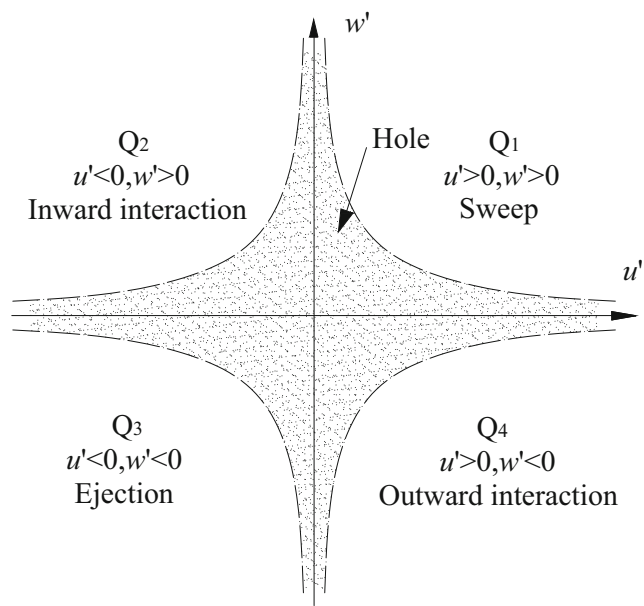
Fig. 10 Diagram for four quadrants with the "hole" region ($0.24 < z/h_g < 2.4$)
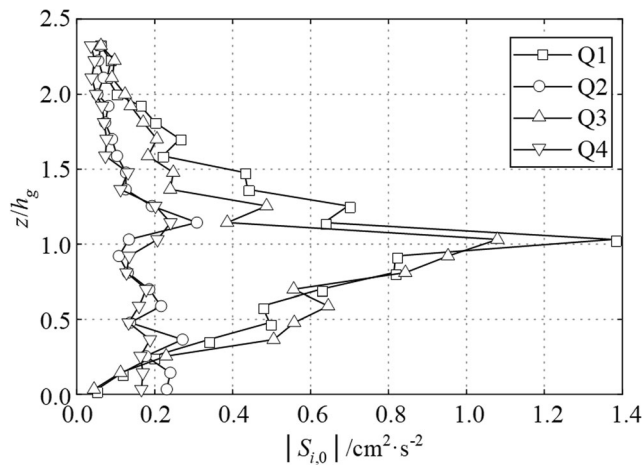
Fig. 11 Contributions from each quadrant to the Reynolds stresses when the threshold value H_0 is zero at $x/L_{veg} = 0.80$

where

$$C_{i,H_0}(t) = \begin{cases} 1, & \left|u'(t)w'(t)\right| > H_0\left|\overline{u'w'}\right| \text{ and } \left[u'(t), w'(t)\right] \text{ in the quadrant } Q_i, \\ 0, & \text{otherwise} \end{cases}$$

(5)

where T is the recording time and $u'(t)$ and $w'(t)$ are the fluctuating velocities in the streamwise and vertical directions for each measured point, respectively. By definition, S_{1,H_0} and S_{3,H_0} are positive, whereas S_{2,H_0} and S_{4,H_0} are negative.

The vertical profile of $S_{i,0}$ in fully developed flow zone at $x/L_{veg} = 0.80$ is shown in Fig. 11. In the equilibrium zone, ejections (Q3) and sweeps (Q1) were the primary contributions to the momentum exchange near the water–canopy interface. The contributions of ejections (Q3) and sweeps (Q1) to the Reynolds stresses reached a maximum at the water–canopy interface ($z/h_g = 1.0$) and presented a decrease trend from the interface toward the water surface and flume bed. The contributions of sweeps (Q1) to the Reynolds stresses outweighed that of ejections (Q3) in the lower layer of root canopies ($1.0 < z/h_g < 2.0$). This finding indicated that the sweep event (Q1) was the dominant flow type in this region, whereas the relationship was opposite in the upper layer of the gap region ($0.24 < z/h_g < 1$), as shown in Fig. 13. Similar with

the conventional boundary layer flow, ejections (Q2) and sweeps (Q4) were the dominant flow types in the lower layer of the gap region ($0 < z/h_g < 0.24$). The contributions of quadrants Q2 and Q4 to the Reynolds stress were positive, whereas Q1 and Q3 were negative. Quadrants Q2 and Q4 outweighed Q1 and Q3 in the lower layer of the gap region at $0 < z/h_g < 0.24$, as shown in Figs. 11 and 12b. Thus, the signs of Reynolds stress were positive, which was mainly caused by the channel bed effect. However, the signs Reynolds stress were negative at the interface ($z/h_g = 1.0$).

Figure 13 illustrates the development of ratios of the sweep to ejection events $\left|S_{S,H_0}\right|/\left|S_{E,H_0}\right|$ and ratios of the sweep and ejection events to inward and outward interactions $\left(\left|S_{S,H_0}\right| + \left|S_{E,H_0}\right|\right)/\left(\left|S_{I,H_0}\right| + \left|S_{O,H_0}\right|\right)$ across the vertical direction at $x/L_{veg} = 0.80$. The experimental flow was fully developed to reveal their relation, which Fig. 11 may not reveal directly. With regard to the ratios of the sweep and ejection events to inward and outward interactions, the former was prominent, especially at the water–canopy interface. However, the ratio of the sweep events gradually decreased toward the top of root canopies and flume bottom.

For varying threshold values H_0, the development of $\left(\left|S_{S,H_0}\right| + \left|S_{E,H_0}\right|\right)/\left(\left|S_{I,H_0}\right| + \left|S_{O,H_0}\right|\right)$ seemed quite different. As shown in Fig. 14, the profile ratios of the sweep and ejection events to inward and outward interactions were presented for various values of H_0 ranging from 0 to 5. The contributions of sweeps and ejections to the Reynolds stresses inside the root canopy and near the channel bed were roughly equivalent to that of inward and outward interactions. The contribution of sweeps and ejections near the water–canopy interface was significantly greater than that of inward and outward interactions. With the increasing H_0, the ratio $\left(\left|S_{S,H_0}\right| + \left|S_{E,H_0}\right|\right)/\left(\left|S_{I,H_0}\right| + \left|S_{O,H_0}\right|\right)$ gradually increased especially at the lower layer of root canopy, upper layer of gap region, and near the flume bed. This finding indicated the predominant contributions of sweeps and ejections to the Reynolds stresses. The hole domain gradually eliminated small values of the Reynolds stresses in four

Fig. 12 Different flow types in four quadrants **a** at the water–canopy interface ($z/h_g = 1.06$) and **b** near the flume bed ($z/h_g = 0.03$) at $x/L_{veg} = 0.80$; the dashed lines represent hyperbolae corresponding to $\left|u'w'\right| = H_0\left|\overline{u'w'}\right|$, where $H_0 = 1$
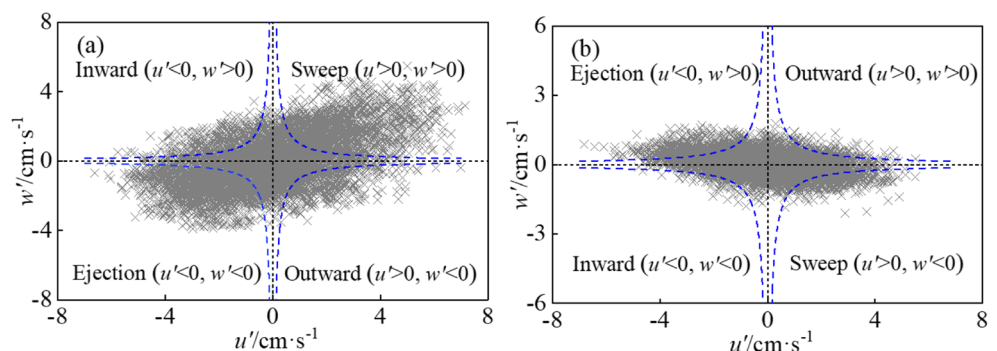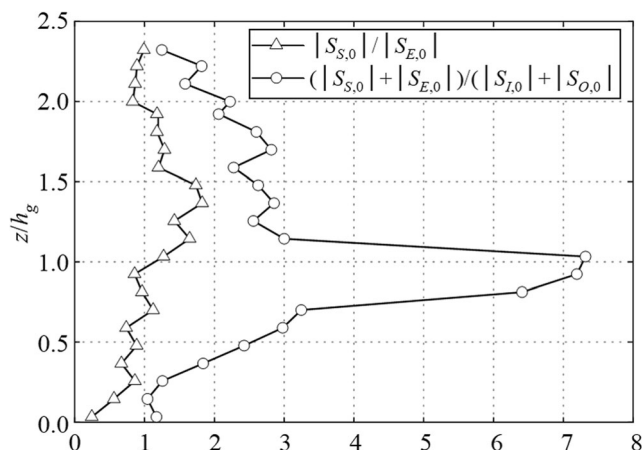
Fig. 13 Ratios of contributions of different quadrants to momentum exchange across a representative flume vertical direction at $x/L_{veg} = 0.80$

quadrants with the hole scale increasing. The contributions of sweeps and ejections to the Reynolds stress were larger than that of inward and outward interactions when the threshold $H_0 = 0$ at the water–canopy interface. Thus, the removal of small events from four quadrants made the contributions of ejections and sweeps greater than that of inward and outward interactions.

The contributions of the ejection and sweep events to the Reynolds stresses at the water–canopy interface for various threshold values are normalized, wherein H_0 was changing from 0 to 8, which can be formulated as:

$$S^*(H_0) = \left(S_{1,H_0} + S_{3,H_0}\right) / \left(S_{1,0} + S_{3,0}\right) \qquad (6)$$

$T^*(H_0)$ is the ratio of the sweep and ejection events to total duration time, which can be formulated as:

$$T^*(H_0) = \frac{1}{T} \int_0^T \left(C_{1,H_0}(t) + C_{3,H_0}(t)\right) dt \qquad (7)$$
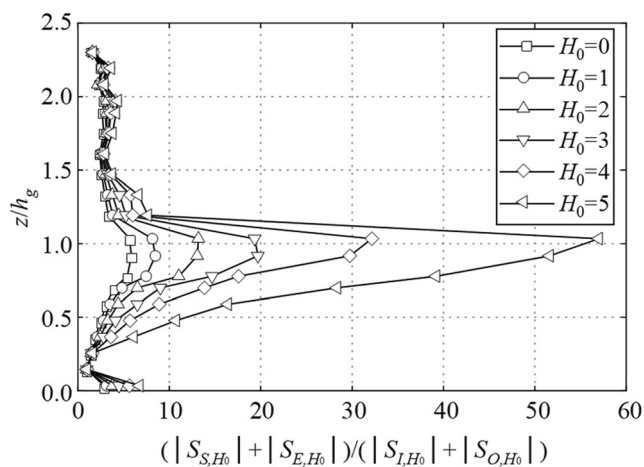

Fig. 14 Ratio $\left(\left|S_{S,H_0}\right| + \left|S_{E,H_0}\right|\right) / \left(\left|S_{I,H_0}\right| + \left|S_{O,H_0}\right|\right)$ for various thresholds H_0 at $x/L_{veg} = 0.80$

A relation between $S^*(H_0)$ and $T^*(H_0)$ was established and shown in Fig. 15, where S^* revealed the proportion of contribution of the ejection and sweep events larger than the threshold value $H_0 \left|\overline{u'w'}\right|$. T^* indicated the ratio of time taken to generate sweeps and ejections, which were normalized by the total recording time. In this experiment, approximately 80% of the sweep and ejection events at the water–canopy interface occupied within only 30% of the sampling time. Moreover, $T^*(0) \approx 0.7$ when $S^*(0) = 1$, indicating that the inward and outward interactions occurred within only 30% of the total sampling time.

Conclusion

The results and conclusion of this study are presented as follows:

(1) The existence of root canopy caused a discontinuous drag force in the vertical direction, which resulted in a vertical variation of the time-averaged streamwise velocity with an inflection point (fast in gap region, whereas slow inside root canopy). As a result, coherent vortex structures were induced at the bottom of root canopy. According to the flow characteristics, these structures can be classified into three distinct domains, namely, the initial adjustment flow, developing, and fully developed zones. The equilibrated vertical Reynolds stresses and T_{KE} reached their maximum values at the water–canopy interface and gradually decreased toward the water surface and channel bed, respectively. Positive Reynolds stresses were measured at the lower layer of gap region, which is in agreement with the results of the quadrant analysis that the contributions of Q2 (ejections) and Q4 (sweeps) to the Reynolds stresses had dominated in the same region.
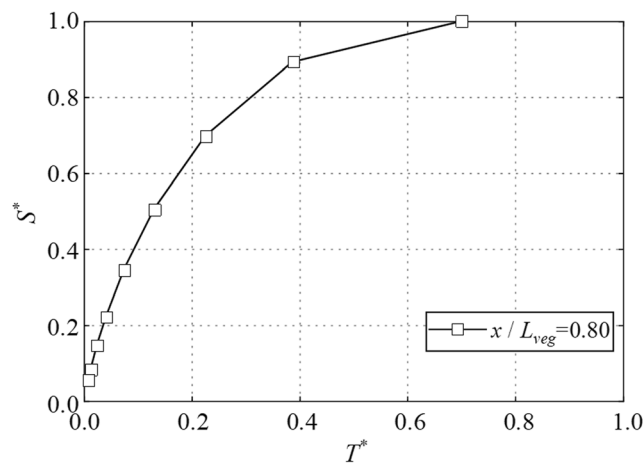
Fig. 15 Relationship between the ratio of sweeps and ejections and fractional time at $x/L_{veg} = 0.80$

(2) The development of the momentum thickness in the flow direction is the same as that of the width of a canonical mixing layer. These length scales grew originally and then stabilized at equilibrated flow region. The inflection in the time-averaged streamwise velocity in the vertical direction generated a coherent vortex structure. In the mixing layer, the dominant frequency of this vortex was determined using spectral analysis. When frequencies were normalized using the local momentum thickness $\theta(x)$ and velocity $\langle U \rangle$, one single dominant frequency had emerged in the flow direction. Two types of vortices had dominated different areas, namely, shear-scale (large-scale) and stem-scale (small-scale) vortices.

(3) The sweeps and ejections had dominated in the whole vertical direction. The sweep events were greater than the ejection events in the lower layer of root canopies. However, the relationship was reversed in the gap region. Sweeps and ejections were brief and intense. Approximately 80% of sweeps and ejections were completed within 30% of the record period near the bottom of root canopies (i.e., the position of the maximum Reynolds stress).

Nomenclature The following symbols were used in this paper: a, root canopy density (m^{-1}); n, number of cylinders per bed area (m^{-2}); d, cylinder diameter (m); s, vegetation spacing (m); S_0, channel bed slope (vertical:horizontal) (-); Q, flow rate (m^3/s); b, width of floating vegetated islands (m); B, flume width (m); h_r, height of root canopy (m); h_g, height of gap region (m); H, flow depth (m); H_p, Penetration depth (m); L_{veg}, length of floating vegetated islands (m); ν, Kinematic viscosity (m^2/s); g, Gravitational acceleration (m/s^2); x, y, z, streamwise, lateral and vertical directions (-); U, V, W, time-averaged velocity components in x, y, z directions (m/s); u, v, w, instantaneous velocity components in x, y, z directions (m/s); u', v', w', fluctuating velocities in x, y, z directions (m/s); u_{*b}, bulk friction velocity (m/s); U_m, cross-sectional average streamwise velocity of the flow (m/s); U_a, characteristic streamwise velocity in Eq. (3) (m/s); U_{d1}, stable time-averaged streamwise velocity in high-stream velocity layer (m/s); U_{d2}, stable time-averaged streamwise velocity in low-stream velocity layer (m/s); $\langle U \rangle$, arithmetic average of U_{d1} and U_{d2} (m/s); ΔU, velocity difference between U_{d1} and U_{d2} (m/s); Re, bulk Reynolds number (-); Fr, bulk Froude number (-); St, Strouhal number (-); R_H, hydraulic radius (m); T_{KE}, turbulent kinetic energy (m^2/s^2); θ, momentum thickness (m); δ, mixing layer thickness (m); $-\overline{u'w'}$, Reynolds stress with respect to vertical plane (m^2/s^2); S_{ww}, power spectral density (cm^2/s); H_0, threshold value (-); S_{i,H_0}, contribution of various flow types to Reynolds stress (cm^2/s^2); $C_{i,H_0}(t)$, averaging condition in Eq. (4)

References

Ai YD, Liu MY, Huai WX (2020) Numerical investigation of flow with floating vegetation island. Journal of Hydrodynamics 32(1):31–43

Borne KE (2014) Floating treatment wetland influences on the fate and removal performance of phosphorus in stormwater retention ponds. Ecol Eng 69:76–82

Downing-Kunz M, Stacey M (2011) Flow-induced forces on free-floating macrophytes. Hydrobiologia 671(1):121–135

Ghisalberti M, Nepf HM (2002) Mixing layers and coherent structures in vegetated aquatic flows. J Geophys Res Oceans 107(C2):3011

Ghisalberti M, Nepf HM (2004) The limited growth of vegetated shear layers. Water Resour Res 40:W07502

Goring DG, Nikora VI (2002) Despiking acoustic Doppler velocimeter data. J Hydraul Eng-ASCE 128(1):117–126

Keddy PA (2010) Wetland ecology: principles and conservation, 2nd edn. Cambridge University Press, New York, pp 313–314

Li SL, Katul G, Huai WX (2019) Mean velocity and shear stress distribution in floating treatment wetlands: an analytical study. Water Resources Research 55:6436–6449

Lin YF, Jing SR, Wang TW, Lee DY (2002) Effects of macrophytes and external carbon sources on nitrate removal from groundwater in constructed wetlands. Environ Pollut 119(3):413–420

Liu C, Shan YQ, Lei JR, Nepf HM (2019) Floating treatment islands in series along a channel: the impact of island spacing on the velocity field and estimated mass removal. Advances in Water Resources 129:222–231

Lu SS, Willmarth WW (1973) Measurements of the structure of the Reynolds stress in a turbulent boundary layer. J Fluid Mech 60: 481–511

Nahlik AM, Mitsch WJ (2006) Tropical treatment wetlands dominated by free-floating macrophytes for water quality improvement in Costa Rica. Ecol Eng 28(3):246–257

Nepf HM, Vivoni ER (2000) Flow structure in depth-limited, vegetated flow. J Geophys Res-Oceans 105(C12):28547–28557

Nichols P, Lucke T, Drapper D, Walker C (2016) Performance evaluation of a floating treatment wetland in an urban catchment. Water 8(6)

Nikora V (2010) Hydrodynamics of aquatic ecosystems: an interface between ecology, biomechanics and environmental fluid mechanics. River Res Appl 26(4):367–384

Nikora VI, Goring DG (1998) ADV measurements of turbulence: can we improve their interpretation? J Hydraul Eng-ASCE 124(6):630–634

Plew DR (2011) Depth-averaged drag coefficient for modeling flow through suspended canopies. J Hydraul Eng-ASCE 137:234–247

Plew DR, Spigel RH, Stevens CL, Nokes RI, Davidson MJ (2006) Stratified flow interactions with a suspended canopy. Environ Fluid Mech 6:519–539

Poggi D, Katul GG, Albertson JD (2004) Momentum transfer and turbulent kinetic energy budgets within a dense model canopy. Bound-Layer Meteor 111(3):589–614

Poindexter CM, Rusello PJ, Variano EA (2011) Acoustic Doppler velocimeter-induced acoustic streaming and its implications for measurement. Exp Fluids 50(5):1429–1442

Raupach MR, Thom AS (1981) Turbulence in and above plant canopies. Annu Rev Fluid Mech 13:97–129

Raupach MR, Finnigan JJ, Brunei Y (1996) Coherent eddies and turbulence in vegetation canopies: the mixing-layer analogy. Bound-Layer Meteor 78:351–382

Rogers MM, Moser RD (1994) Direct simulation of a self-similar turbulent mixing layer. Phys Fluids 6(2):903–923

Sanford LP, Crawford SM (2000) Mass transfer versus kinetic control of uptake across solid-water boundaries. Limnol Oceanogr 45:1180–1186

Schlichting H, Gersten K (2017) Boundary-layer theory, 9nd edn. McGraw-Hill, New York, p 21

Stewart FM, Mulholland T, Cunningham AB, Kania BG, Osterlund MT (2008) Floating islands as an alternative to constructed wetlands for treatment of excess nutrients from agricultural and municipal wastes–results of laboratory-scale tests. Land Contamination & Reclamation 16(1):25–33

Tanner CC, Sukias J, Park J, Yates C, Headley TR (2011) Floating treatment wetlands: a new tool for nutrient management in lakes and waterways. Methods

Toft JD, Simenstad CA, Cordell JR, Grimaldo LF (2003) The effects of introduced water hyacinth on habitat structure, invertebrate assemblages, and fish diets. Estuaries 26(3):746–758

Welch PD (1967) The use of fast Fourier transform for the estimation of power spectra: a method based on time averaging over short, modified periodograms. IEEE Transact Audio Electroacoustics 15(2): 70–73

White BL, Nepf HM (2007) Shear instability and coherent structures in shallow flow adjacent to a porous layer. J Fluid Mech 593:1–32